1 **Microtubule-associated IQD9 guides cellulose synthase velocity to shape seed mucilage**

2

3 Bo Yang[1], Gina Stamm[2], Katharina Bürstenbinder[2,*], Cătălin Voiniciuc [1,*]

4

5 [1]Independent Junior Research Group–Designer Glycans, Leibniz Institute of Plant

6 Biochemistry, 06120 Halle (Saale), Germany; [2]Department of Molecular Signal Processing,

7 Leibniz Institute of Plant Biochemistry, 06120 Halle (Saale), Germany;

8

9 *Authors for correspondence:

10 Katharina Bürstenbinder

11 Tel: +49 345 5582 1226

12 E-Mail: Katharina.Buerstenbinder@ipb-halle.de

13

14 Cătălin Voiniciuc

15 Tel: +49 345 5582 1720

16 E-Mail: Catalin.Voiniciuc@ipb-halle.de

17

18

19

20 **E-Mails and ORCiD**

B.Y.	Bo.Yang@ipb-halle.de	0000-0003-4446-0415
G.S.	Gina.Stamm@ipb-halle.de	
K.B.	Katharina.Buerstenbinder@ipb-halle.de	0000-0002-3493-4800
C.V.	Catalin.Voiniciuc@ipb-halle.de	0000-0001-9105-014X

21

22

23

24 **Total word count for the main body of the text:** 5908

25 **Summary:** 228; **Introduction:** 798; **Materials and Methods:** 1695; **Results:** 1579 words;

26 **Discussion:** 1625; **Acknowledgements:** 92

27 **Number of figures: 7** (all in color)

28 **Number of tables:** 0

29 **No of Supporting Information files:** 11 in a single PDF (Fig. S1 – S9; Tables S1, S2)

30 **Summary**

31

32 ● Arabidopsis seeds release large capsules of mucilaginous polysaccharides, which are
33 shaped by an intricate network of cellulosic microfibrils. Cellulose synthase complexes is
34 guided by the microtubule cytoskeleton, but it is unclear which proteins mediate this
35 process in the seed coat epidermis (SCE).

36

37 ● Using reverse genetics, we identified *IQ67 DOMAIN 9* (*IQD9*) and *KINESIN LIGHT*
38 *CHAIN-RELATED 1* (*KLCR1*) as two highly expressed genes during seed development
39 and comprehensively characterized their roles for cell wall polysaccharide biosynthesis
40 and cortical microtubule (MT) organization.

41

42 ● Mutations in *IQD9* as well as in *KLCR1* lead to compact mucilage capsules with aberrant
43 cellulose distribution, which can be rescued by transgene complementation. Double
44 mutant analyses revealed that their closest paralogs (*IQD10* and *KLCR2*, respectively) are
45 not required for mucilage biosynthesis. IQD9 physically interacts with KLCR1 and
46 localizes to cortical MTs to maintain their organization in SCE cells. Similar to the
47 previously identified TONNEAU1 (TON1) RECRUITING MOTIF 4 (TRM4) protein,
48 IQD9 is required to maintain the velocity of cellulose synthases.

49

50 ● Our results demonstrate that IQD9, KLCR1 and TRM4 are MT-associated proteins that
51 are required for seed mucilage architecture. This study provides the first direct evidence
52 that members of the IQD, KLCR and TRM families have overlapping roles in guiding the
53 distribution of cell wall polysaccharides. Therefore, SCE cells provide an attractive system
54 to further decipher the complex genetic regulation of polarized cellulose deposition.

55

56 **Key words**: Arabidopsis thaliana, cellulose synthesis, cortical microtubules, matrix
57 polysaccharides, scaffold proteins, seed mucilage, plant cell wall

Introduction

The seed coat epidermal (SCE) cells of some Angiosperms, including the model plant *Arabidopsis thaliana*, synthesize large amounts of hydrophilic polysaccharides (North *et al.*, 2014; Voiniciuc *et al.*, 2015c; Šola *et al.*, 2019). Although the mucilage capsules that rapidly encapsule Arabidopsis seeds upon hydration are pectin-rich, they can be regarded as specialized secondary cell walls because they also contain hemicelluloses that are typical of woody tissues (Voiniciuc *et al.*, 2015c). Substituted xylans and heteromannans maintain the attachment of mucilaginous pectin to the seed surface and the organization of ray-like cellulose microfibrils (Yu *et al.*, 2014; Voiniciuc *et al.*, 2015b,a; Hu *et al.*, 2016; Ralet *et al.*, 2016). Upon imbition of a dry seed, expanding mucilage ruptures the outer primary cell wall to release a two-layered gelatinous capsule that can be visualized by ruthenium red (RR), a pectin-binding dye. Cellulosic rays extend from the top of each SCE cell to intertwine and anchor the inner, adherent mucilage layer to the seed surface (Sullivan *et al.*, 2011; Mendu *et al.*, 2011; Harpaz-Saad *et al.*, 2011). However, the genetic factors that modulate the deposition of highly ordered cellulosic structures in seed mucilage remain largely unknown.

The current dogma is that plant crystalline microfibrils are produced by rosette-shaped cellulose synthase (CESA) complexes (CSC) composed of at least three different CESA isoforms and a growing number of interacting proteins (Polko & Kieber, 2019). In Arabidopsis SCE cells, mutations in *CESA3* and *CESA5* have been shown to affect the deposition of cellulose in mucilage pockets. Loss-of-function *cesa5* mutants have a nearly complete loss of adherent mucilage due to reduced cellulose production (Sullivan *et al.*, 2011; Mendu *et al.*, 2011; Harpaz-Saad *et al.*, 2011), while *cesa3* missense mutants lead to milder alterations of mucilage adherence and cellulose organization (Griffiths *et al.*, 2015). Several accessory proteins are also known to influence mucilage cellulose synthesis. COBRA-LIKE2 (COBL2) contains a glycosyl-phosphatidylinositol (GPI) anchor and facilitates the assembly of crystalline cellulose by CESA5 (Ben-Tov et al., 2015), while FEI2 (meaning "fat" in Chinese) and SALT-OVERLY SENSITIVE5 (SOS5) mediate pectin adherence to cellulosic rays via an independent mechanism (Griffiths *et al.*, 2014, 2016; Ben-Tov *et al.*, 2018). CSC assembly and trafficking are maintained by STELLOs (Greek for "to send"; Zhang *et al.*, 2016), and negatively regulated by SHOU4 ("thin" in Chinese; Polko *et al.*, 2018), identified via a screen for *fei2* suppressors.

Cortical microtubules (MTs) can orient cellulose microfibril deposition by positioning the delivery of CSCs to the plasma membrane (PM) and guiding their subsequent trajectories (Paredez *et al.*, 2006; Gutierrez *et al.*, 2009; Bringmann *et al.*, 2012a). MT-associated proteins,

92   which shape the cytoskeleton in response to environmental or developmental signals (Lloyd &
93   Hussey, 2001; Sedbrook & Kaloriti, 2008), can influence the organization of mucilage
94   polysaccharides. A   temperature-sensitive   point   mutation   in   *MICROTUBULE*
95   *ORGANIZATION 1* (*MOR1*) significantly reduced mucilage release at 29°C (McFarlane *et al.*,
96   2008). A second MT-associated protein, TONNEAU1 (TON1) RECRUITING MOTIF 4
97   (TRM4), was recently found to organize cortical arrays and cellulose distribution (Yang *et al.*,
98   2019). The *trm4* seed mucilage capsules are compact and have shorter cellulosic rays compared
99   to the WT, without altering pectin adherence. Arabidopsis CESAs circle around the
100 cytoplasmic column of SCE cells to polarly deposit cellulose microfibrils in mucilage pockets
101 (Griffiths *et al.*, 2015), but the network of proteins that guide CESAs in SCE cells remains
102 unclear.

103   Plant-specific IQ67 DOMAIN (IQD) proteins associate with MTs and have scaffold-like
104 properties (Bürstenbinder *et al.*, 2017). Their eponymous IQ67 domain contains 67 amino acids
105 with calmodulin-recruiting motifs (Abel *et al.*, 2005), which could be involved in Ca^{2+}
106 signaling integration (Kölling *et al.*, 2019). Since multiple Arabidopsis IQDs control cell shape
107 and size (Bürstenbinder *et al.*, 2017; Liang *et al.*, 2018; Mitra *et al.*, 2019), they are
108 hypothesized to support cell wall deposition. Certain IQDs interact with KINESIN LIGHT
109 CHAIN-RELATEDs (KLCRs; Bürstenbinder *et al.*, 2013; Zang *et al.*, 2021) proteins. KLCRs
110 are also known as CELLULOSE SYNTHASE-MICROTUBULE UNCOUPLING (CMU) and
111 stabilize MTs at the PM during cellulose synthesis (Liu *et al.*, 2016). However, direct evidence
112 for how IQDs influence the biosynthesis of cell wall polysaccharides has been lacking.

113   In this study, we identified IQD9 and KLCR1 as two additional players that maintain
114 MT organization and the deposition of ray-like cellulosic microfibrils in SCE cells. In the
115 absence of *IQD9* or *KLCR1*, mutant seeds released compact mucilage capsules due to
116 aberrant deposition of cellulose microfibrils as previously observed for *trm4* lines. IQD9
117 physically interacted *in vivo* with KLCR1 and formed filamentous arrays. Live-cell imaging
118 showed that IQD9 and KLCR1 are localized a circular pattern during mucilage biosynthesis,
119 which is reminiscent of CSC trajectories . Both *iqd9* and *trm4* mutants displayed slower
120 CESA3 particles in SCE cells, indicating that these MT-associated proteins guide cellulose
121 deposition. IQD, KLCR and TRM proteins therefore have overlapping roles in cell wall
122 biosynthesis.

123

124 **Materials and Methods**

125 **Plant materials and growth conditions**

126   *Arabidopsis thaliana* Col-0 (WT) and T-DNA insertion mutants (Table S1) analyzed in

127   this study were obtained from the Nottingham Arabidopsis Stock Centre, unless otherwise

128   noted. The *proUBQ:RFP-TUB6* in Col-0 (Ambrose *et al.*, 2011), *proCESA3:GFP-CESA3* in

129   *je5* mutant (Desprez *et al.*, 2007) and *pKLCR1:KLCR1-GFP* in *klcr1-1* (Zang *et al.*, 2021)

130   transgenic plants have been described previously. Arabidopsis plants were grown in a

131   phytochamber with constant light (100–120 µmol m^{-2} s^{-1}), 22°C and 60% humidity.

132   *Nicotiana benthamiana* plants were grown in a greenhouse (16 h light, 8 h dark) at 22–24°C.

133

134   **Arabidopsis transcriptional analyses**

135   Total RNA was isolated from 10-day-old seedlings using TRI Reagent (Sigma Aldrich),

136   according to its manual. The cDNA was prepared from 4 µg of RNA using RevertAid reverse

137   Transcriptase (Thermo Fisher Scientific), and reverse transcription polymerase chain reaction

138   (RT-PCR) was performed using primers listed in Table S2. *ACTIN2* served as a housekeeping

139   gene, and WT genomic DNA was included as a control.

140   For GUS staining, sample tissues (seedlings, flower buds, siliques) were fixed in 80%

141   (v/v) ice-cold acetone for 30 min and incubated for 4 h to overnight in GUS staining solution

142   (50 mM sodium phosphate, pH 7.2, 0.5 mM $K_3Fe(CN)_6$, 0.5 mM $K_4Fe(CN)_6$, 2 mM 5-bromo-

143   4-chloro-3-indolyl-β-glucuronic acid, 10 mM EDTA) at 37 °C. Images were acquired using a

144   Zeiss Axioplan 2 microscope or a Nikon SMZ 1000. For GUS staining of Arabidopsis seeds,

145   siliques of different ages were opened with forceps at the replum. Seeds were collected with a

146   small spoon and transferred to a 1.5 ml tube with staining solution. Prior to DIC microscopy,

147   staining solution was removed and samples were mounted in chloralhydrate.

148

149   **Plasmid construction and plant transformation**

150   Primers used for plasmid construction are listed in Table S2. *Promoter*:*GFP-GUS*

151   constructs were generated by integrating 1.4 kb of the *IQD9* or *IQD10* promoter into

152   pBGWFS7 (Karimi *et al.*, 2002). The *pIQD9:IQD9-GFP* transgene was assembled using full-

153   length genomic DNA (from ~1.5 kb upstream of ATG up to, but excluding, the *IQD9* stop

154   codon) into pB7FWG0 vector. The constructs were stably transformed into Arabidopsis WT

155   plants (for *pIQD:GFP-GUS*) or *iqd9 iqd10* double mutant (for *pIQD9:IQD9-GFP*)

156   respectively via *Agrobacterium*-mediated floral dip transformation. The *p35S:IQD9-GFP*,

157   *p35S:mCherry-KLCR1,* and *p35S:RFP-KLCR1* transgenes for *N. benthamiana* assays were

158   cloned using Gateway into pB7FWG2 (Karimi *et al.*, 2002), pJOG393 (Gantner *et al.*, 2018)

159   or pGWB455 (Nakagawa *et al.*, 2007) vectors, respectively. The mCherry- and RFP-tagged

5

160 KLCR1 showed similar results. The *pUBQ10:RFP-TUB6* plasmid for transient expression

161 was previously generated (Yang *et al.*, 2019). Transient expression was performed in *N.*

162 *benthamiana* leaves as previously described (Grefen *et al.*, 2010). In short, *Agrobacterium*

163 *tumefaciens GV3101* cells containing the desired constructs were mixed with the P19 viral

164 suppressor (OD600 = 0.7 for each) and incubated for 4 h (at 18 °C, 200 rpm) before

165 infiltration into the lower side of leaves from 5-week-old plants.

166

167 **Staining and quantification of mucilage area**

168 Around 30 seeds were hydrated in water for 30 min and stained with 300 µl of 0.01%

169 (w/v) RR (Sigma-Aldrich; R2751) for 15 min at 125 rpm in 24-well plates. After rinsing with

170 water, the stained seeds were re-suspended in 300 µl of water and imaged with a Leica

171 M165FC stereomicroscope equipped with MC170 HD camera. The mucilage and seed

172 projected areas were quantified using an existing ImageJ pipeline (Voiniciuc *et al.*, 2015b).

173 Cellulose around hydrated seeds was stained with 0.01% (w/v) Pontamine fast scarlet 4B

174 (S4B, also known as Direct Red 23 [Sigma-Aldrich; 212490]) in 50 mM NaCl for 60 min at

175 125 rpm in 24-well plates (Anderson *et al.*, 2010; Mendu *et al.*, 2011). The counterstain was

176 performed by mixing with 25 ug mL^{-1} Calcofluor (Megazyme C-CLFR) for 5 min. Seeds

177 were imaged with a Carl Zeiss LSM 780 microscope with 10X/0.45 objective and the

178 following excitation / emission wavelengths (S4B: 561 / 580–650 nm; Calcofluor: 405 / 410–

179 452 nm). The lengths of cellulosic rays were measured by ImageJ.

180 To view surface morphology, around 30 seeds were mixed with 500 µL of 0.01% (w/v)

181 propidium iodide for 15 min. Seeds were rinsed twice with water and imaged using a Leica

182 LSM 900 with 10X/0.3 objective (excitation 488 nm, emission 600-650 nm).

183

184 **Seed polysaccharide quantification**

185 Non-adherent mucilage was extracted by gently mixing 5 mg seeds in water for 30 min

186 at 125 rpm and subsequently the adherent mucilage was isolated using a ball mill (Retsch;

187 MM400) for 30 min at 30 Hz, as previously described (Voiniciuc, 2016). The two mucilage

188 fractions, spiked with ribose and inositol respectively, were hydrolyzed and quantified via

189 high-performance anion exchange chromatography with pulsed amperometric detection

190 (HPAEC-PAD), as described (Voiniciuc & Günl, 2016) with the following changes. HPAEC-

191 PAD was performed on a Metrohm 940 Professional IC Vario, using Metrosep Carb 2-

192 250/4.0 columns and a published gradient (Mielke *et al.*, 2021). Peaks were integrated and

193 calibrated (manually corrected if necessary) in the MagIC Net 3.2 software (Metrohm).

194   Crystalline cellulose was quantified using the Updegraff reagent (Updegraff, 1969) and

195   the anthrone colorimetric assay (Foster *et al.*, 2010), as previously adapted for Arabidopsis

196   whole seeds (Voiniciuc *et al.*, 2015b).

197

198   **Salt stress treatments**

199   Germination assays were performed in 24-well culture plates as described previously

200   (Yang et al., 2021). Around 35 seeds were hydrated in 500 µl of water or 150 mM $CaCl_2$

201   solution per well. All the seeds were vernalized for 66 h (dark, 4°C), transferred to a chamber

202   with constant light (100– 120 µmol m^{-2} s^{-1}), 22°C and 60% humidity. The seeds were imaged

203   every 24 h with a Leica M165FC stereomicroscope and defined as germinated when the

204   radicle length was > 70 µm.

205   For the seedling salt stress assay, the seeds were placed on ½ Murashige and Skoog agar

206   plates, stratified for 66 h (dark, 4°C) and grown vertically in the climate-controlled chamber

207   described above. Five-day-old seedlings of similar size were transferred to fresh agar plates

208   with or without 100 mM NaCl and growth was imaged using a Nikon D5600 digital camera.

209

210   **Stem cell wall analyses**

211   Stem sections were cut by hand from the basal third of stems of 6-week-old plants and

212   were stained in 0.01% toluidine blue O (Sigma-Aldrich; T3260) for 2 min. Stained sections

213   were rinsed twice with water and imaged on a Axioplan 2 with Axiovision software (Zeiss).

214   The bottom 7 cm of mature stems were harvested and homogenized using a ball mill

215   (Retsch MM400) for 10 min at 30 Hz. The AIR was extracted by sequential washes with 1

216   mL of 70% (v/v) ethanol, 1 mL of 1:1 (v/v) chloroform:methanol and 1 mL of acetone. Stem

217   AIR was hydrolyzed and quantified via HPAEC-PAD exactly as described for seed mucilage,

218   using ribose as the internal standard.

219

220   **Confocal microscopy and image analysis**

221   For fluorescence co-localization assays in *N. benthamiana*, leaf discs at 3 days post-

222   infiltration were imaged with a Zeiss LSM880 inverted confocal microscope using a 40X/1.2

223   water-immersion objective. For oryzalin treatment, small pieces of transfected leaf were

224   immersed with 1% (v/v) dimethylsulfoxide (DMSO) as mock treatment or 1% (v/v) DMSO

225   containing 0.1 mM oryzalin (Sigma-Aldrich) for 4 h.

226   For the fluorescence imaging of the Arabidopsis SCE cells, seeds were carefully

227   dissected from siliques at specific stages and were imaged using a Zeiss LSM880 in Airyscan

228 mode with a 40X/1.2 water-immersion objective. For PM, 7 DPA (days post-anthesis) seeds

229 were pre-stained in 50 µM FM4-64 for 30 min before imaging. The subcellular localization

230 of GFP-CESA3 was detected using a 63X/1.4 oil-immersion objective and Airyscan mode,

231 with 330 ms exposure time based on previously described protocols (Vellosillo *et al.*, 2015;

232 Duncombe *et al.*, 2020). Unless stated otherwise, the time-lapse series were acquired every 5

233 sec for 5 min. All the samples were mounted on confocal dishes with spacers (VWR

234 International; 734-2905) and were examined with the following excitation/emission settings:

235 GFP (488 / 505–530 nm), RFP/mCherry (514 / 580–635 nm), FM4-64 (514 / 600–700 nm).

236 For hypocotyl imaging, seeds were sowed on ½ MS agar plates and stratified for 66 h

237 (dark, 4°C). The plates were exposure to light for 6 h at room temperature and then were

238 wrapped with aluminum foil to keep the plates in the dark at room temperature. For the

239 observation of RFP-TUB6 in the hypocotyl epidermal cells, the inner face of epidermal cells

240 in zone 1 of 4-d-old dark-grown seedlings were examined as described previously (Crowell et

241 al., 2011).

242 All images were processed uniformly using ImageJ. The maximum projection of the Z-

243 stack or time-lapse view was generated by frames using the Z Project tool and average

244 intensity. For the colocalization evaluation, the intensity plot analysis was done by "RGB

245 Profile Plot" plugin. The Pearson correlation coefficient of region of interest (ROI) from

246 single frame was quantified with "Coloc 2". Kymograph analysis of proteins and velocity

247 quantification of GFP-CESA3 were performed as previously described (Vellosillo *et al.*,

248 2015). Briefly, the time-lapse stack was generated with "Walking Average" plugin. The GFP-

249 CESA3 track was depicted using segmented line on time average image and transferred to

250 time-lapse stack. The kymographs were generated using the "MultipleKymograph" plugin,

251 and the slope of each line was used to calculate the particle velocity.

252

Protein-Protein Interactions

254 Proteins were extracted from transiently transformed *N. benthamiana* leaves using 1 ml

255 lysis buffer (20 mM HEPES, pH 7.5, 40 mM KCl, 1 mM EDTA, 0.1% [v/v] Triton X-100, 1×

256 protease inhibitor cocktail, 1 mM phenylmethylsulfonyl fluoride, and 10% [v/v] glycerol)

257 (Ganguly *et al.*, 2020). Homogenate from 500 mg of plant material was centrifuged twice at

258 4°C at 15000 g for 10 min, and 900 µl of the supernatant was incubated with 20 µl GFP-Traps

259 (Chromotek) overnight at 4°C on a rocking shaker. Beads were equilibrated following

260 manufacturer's manual using lysis buffer, without Triton-X. The next day, beads were washed

261 four times and were boiled in 80 µl 2x Laemmli Buffer. For each sample, 40 µl were loaded

8

262   on a SDS gel and blotted afterwards for 1 h. For protein detection, 1:1000 dilution of the GFP

263   antibody 3H9 (Chromotek) or the RFP antibody 6G6 (Chromotek) was used. Anti-mouse

264   (Sigma A9044 1:20000) and anti-rat (Thermo 31470 1:3000) secondary antibodies conjugated

265   to horseradish peroxidase were used to detect RFP and GFP signals, respectively. Western blot

266   images were acquired with a FluorChem system, using 1:1 mixture of Amersham ECL-Prime

267   and ECL-Select as chemiluminescent detection reagents.

268

269   **Results**

270   ***IQD9* and *KLCR1* control seed mucilage architecture**

271   We hypothesized that one or more *IQD* genes are involved in Arabidopsis seed mucilage

272   biosynthesis and screened their expression profiles using published transcriptional datasets.

273   *IQD9* (At2G33990) and *IQD10* (At3G15050), its closest paralog, were upregulated in the seed

274   coat at the stages of mucilage biosynthesis (Fig. 1a; Winter *et al.*, 2007; Le *et al.*, 2010). T-

275   DNA insertions in these genes disrupted their transcription (Fig. 1b) and were screened for

276   seed mucilage defects. While *iqd10* mutant seeds resembled WT, two independent *iqd9*

277   mutants displayed compact RR-stained mucilage capsules (Fig. 1c). Consistent with

278   microarray data and the seed mucilage defects (Fig. 1), *promoter*:GUS reporter assays only

279   showed high seed coat activity for *pIQD9* (Fig. S1). *IQD9* and *IQD10* displayed partially

280   overlapping expression profiles but share only 47% amino acid identity (Fig. S1). Furthermore,

281   *iqd9-1 iqd10-1* (*i9 i10*) double mutant seeds showed compact mucilage capsules resembling

282   the *iqd9* single mutants (Fig. 1c).

283   Since IQD-KLCR interactions have been reported (Bürstenbinder *et al.*, 2013), we also

284   assessed if *KLCR1*/*CMU1* (At4g10840) and *KLCR2*/*CMU2* (At3g27960) are involved in

285   mucilage biosynthesis. *KLCR1* was highly expressed throughout the seed development, while

286   *KLCR2* transcription peaks at the pre-globular and globular stages, before mucilage

287   biosynthesis (Fig. S2a). Two knockout *klcr1* alleles, *klcr1-1* and *cmu1* (Fig. S2b, Table S1),

288   resembled the *iqd9* compact mucilage defect (Fig. 1a), while *klcr2* seeds displayed WT-like

289   mucilage. Both *iqd9* as well as *klcr1* mutants reduced mucilage capsule area by 30–40%

290   compared to WT (Fig. 1d), without altering seed size. The double mutant *i9 i10* and *klcr1-1*

291   *klcr2-2* (*k1 k2*) phenocopied the mucilage structure of *iqd9-1* and *klcr1-1* respectively,

292   indicating no functional redundancy between the related genes. Transgene complementation

293   of *i9 i10* with *IQD9* and of *klcr1-1* with *KLCR1* fully rescued the compact mucilage defects

294   (Fig. 1). Both *iqd9* and *klcr1* mutants resembled the mucilage phenotype of *trm4*, which has

295   SCE cells with disorganized MTs (Yang *et al.*, 2019). Moreover, *iqd9 klcr1* and *iqd9 trm4*

9

296   double mutants displayed compact RR-stained mucilage capsules equivalent to the single

297   mutants (Fig. S2c–f).
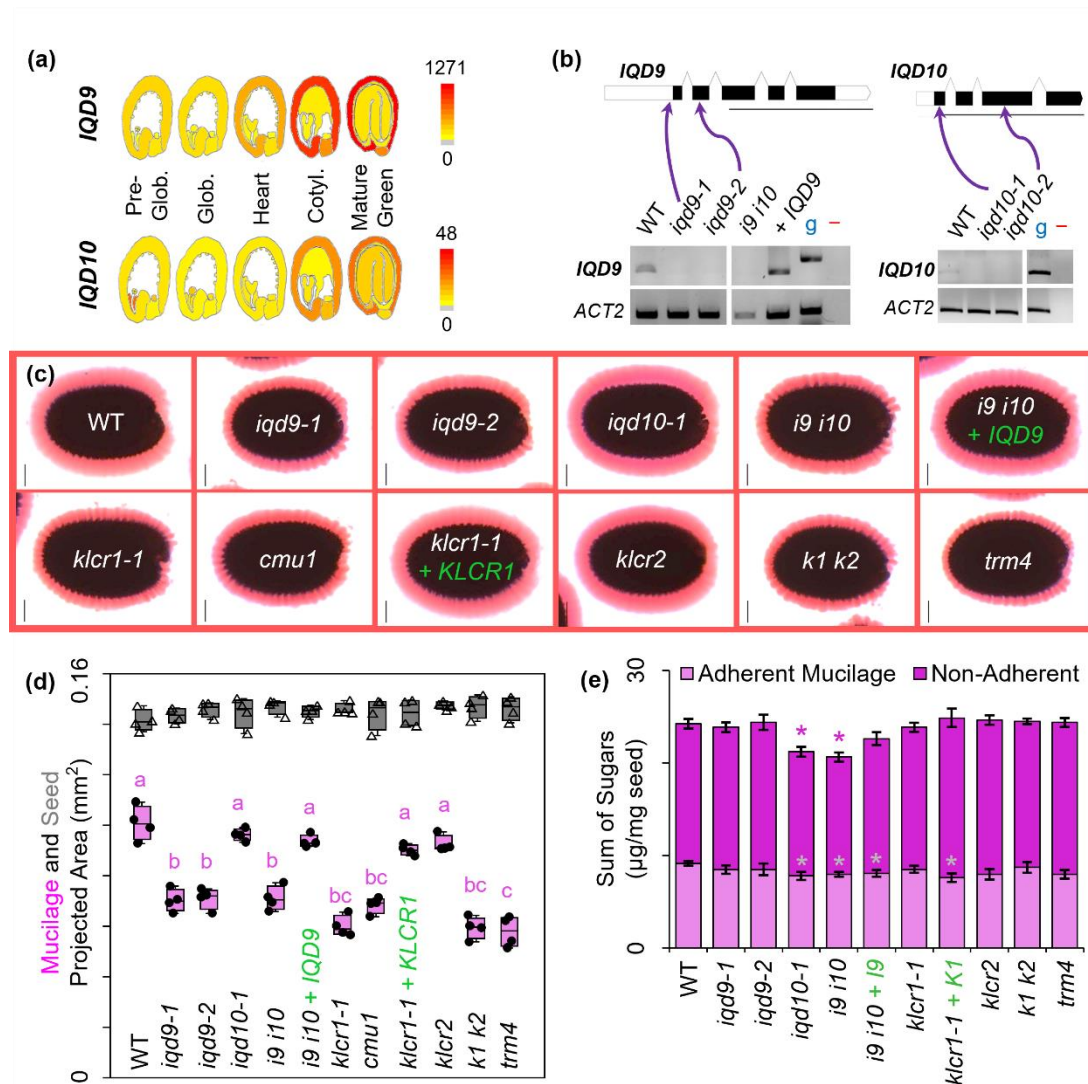
Fig. 1 Mutation of *IQD9* and *KLCR1* caused compact mucilage capsule. (a) Expression profiles in the seed eFP browser (Winter *et al*., 2007; Le *et al*., 2010), including absolute expression values. Glob. (globular); Cotyl. (cotyledon). (b) UTR, intron and exon structure of candidate genes. The position and the effects of T-DNA insertions were verified using RT-PCR, *ACTIN2* as a reference gene, g as genomic DNA control, and – as no DNA control. Transgene complemented were marked by + *IQD* or + *KLCR*. Scale bars for gene models = 1000 bp. (c) RR staining of adherent mucilage capsules after gentle shaking in water. Bars = 100 μm. (d) Seed (triangles) and RR-stained mucilage (black dots) area of four biological replicates (>20 seeds each) per genotype. Boxes show the 25–75% quartiles, the median value (inner horizontal line), and whiskers extending to the largest/smallest values. Different letters mark $P < 0.01$ for one-way ANOVA with Tukey test. (e) Absolute amounts of monosaccharides in sequentially-extracted mucilage fractions. Data show mean $\pm$ SD of 5 biological replicates, and asterisks mark significant changes compared to WT (Student's t-test, $P < 0.001$). See Fig. 2 for detailed composition.

298

IQD9 and *KLCR1* are specifically required for cellulose distribution in mucilage

300   Monosaccharide analysis of non-adherent and adherent mucilage fractions revealed that

301   the *iqd9*, *klcr1* and *trm4* mutants did not alter the content or adherence of matrix

302   polysaccharides to the seed surface (Fig. 1e). Surprisingly, despite no impact on RR staining,

10

303   the *iqd10-1* mutation correlated with a small but statistically significant reduction in total

304   extractable monosaccharides (Fig. 1c–e). The *iqd10-1* mutation decreased rhamnose (Rha)

305   and galacturonic acid (GalA) content in non-adherent mucilage, along with galactose (Gal)

306   and arabinose (Ara) in adherent mucilage (Fig. 2). Nevertheless, compared to the

307   galactoglucomannan-deficient *muci10* mutant with compact mucilage, all the MT-related

308   mutant seeds released relatively normal levels of mucilage glycans (Fig. 2).
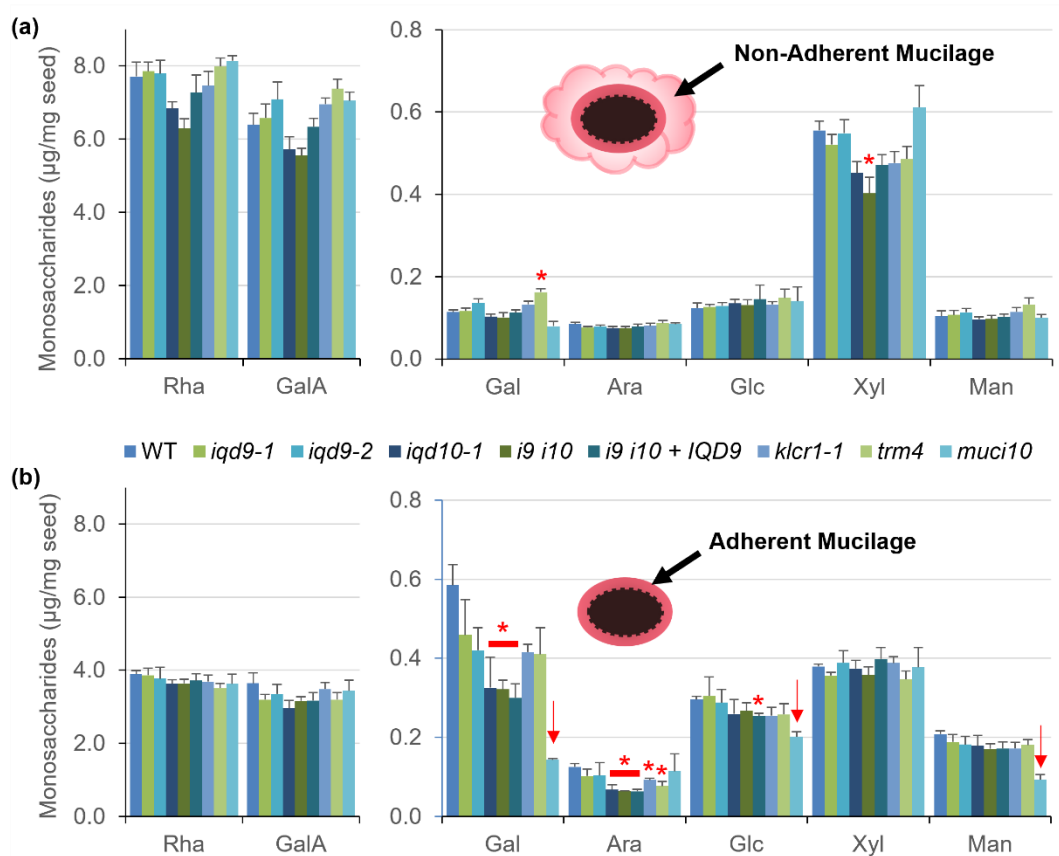

Fig. 2 Composition of matrix polysaccharides in seed mucilage extracts. (a) Non-adherent and (b) adherent mucilage polysaccharides were sequentially extracted using water and different mixing intensities. Data show mean + SD of 5 biological replicates (only 3 for *muci10*). Red asterisks and arrows (for galactoglucomannan subunits) mark differences from WT (Student's t-test, $P < 0.0001$).

309

310   Since the matrix polysaccharide composition could not account for the compact

311   mucilage defects of *iqd9* and *klcr1*, we then examined the structure of cellulose using S4B, a

312   specific fluorescent dye (Anderson et al., 2010). The *iqd9* and *klcr1* mutant seeds extruded

313   less cellulose upon hydration (Fig. 3a) and had ~30% shorter rays atop each columella

314   compared with WT (Fig. 3b). Moreover, the mutant seeds lacked the diffuse cellulose

315   staining that was observed between the WT rays. The S4B-stained seeds of *i9 i10* and *k1 k2*

316   resembled the *iqd9* and *klcr1* single mutants, while *iqd10* and *klcr2* had WT-like seeds. The

317   cellulose defects of *i9 i10* and *klcr1* mutants were rescued by *IQD9* and *KLCR1* transgene

11

318 complementation, respectively, using their native promoters (Fig. 3a). While all the *iqd9*,

319 *klcr1* and *trm4* mutant combinations examined showed short S4B-stained cellulosic rays

320 compared to WT (Fig. 3 and Fig. S3), counterstaining of mucilage with calcofluor displayed

321 relatively normal content of other β-glucans (Fig. S3). Despite evident changes in the

322 architecture of cellulose extruded from hydrated seeds, these MT-related mutants did not alter

323 the crystalline cellulose content of whole seeds (Fig. 3c). Mutations in *IQD9* or *KLCR1* did

324 not alter seed shape (Fig. S4), nor the germination rate or sensitivity to salt (Fig. S5).

325 Therefore, like *TRM4* (Yang *et al.*, 2019), the expression of *IQD9* and *KLCR1* in seeds

326 primarily affect mucilage polymer organization.

327
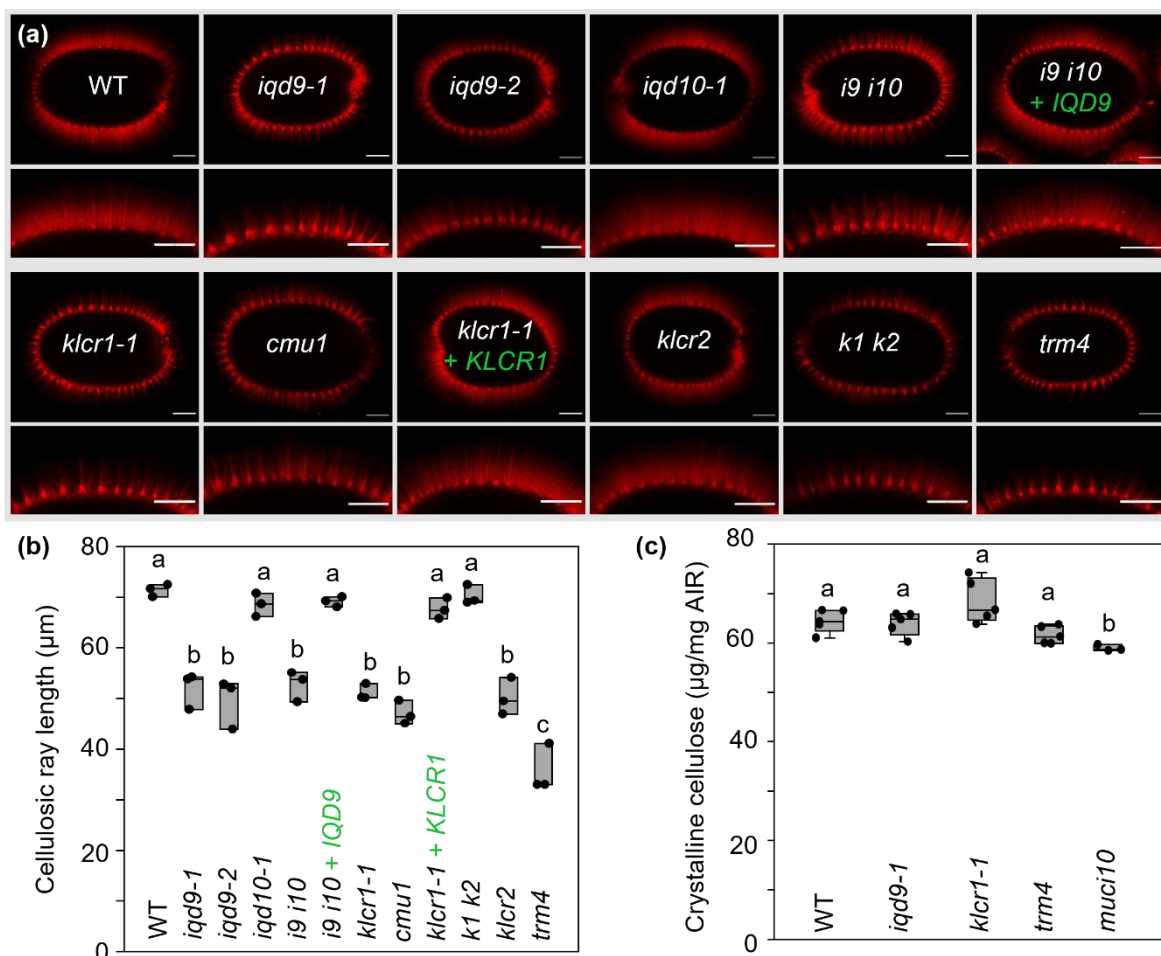
Fig. 3 *IQD9* and *KLCR1* are important for cellulose deposition around seed surface. (a) S4B-stained cellulosic rays in mucilage capsules. Bars = 100 μm. (b) The length of cellulosic rays stained with S4B. Boxes show the 25–75% quartiles, the median value (inner horizontal line), and whiskers extending to the largest/smallest values (≥10 measurements per biological replicate). (c) Crystalline cellulose content in whole seeds (5 biological replicates per genotype, except 3 for *muci10*). Different letters in (b) and (c) mark significant changes (one-way ANOVA with Tukey test, $P < 0.01$).

328

### *IQD9* and *IQD10* are also expressed beyond the seed coat

330 Based on *promoter*:GUS reporter fusions, *pIQD9* and *pIQD10* promoters were active in

331   multiple plant tissues, including the vasculature system (shoot and roots), developing flowers

332   and siliques (Fig. S1). Except for anthers, *pIQD9* showed higher activity than *pIQD10* in

333   reproductive organs and seeds (Fig. S2). *IQD10* was expressed highest in Arabidopsis stems

334   and its ortholog in *Populus deltoides* (*PdIQD10*) affects the development of the woody stem

335   (Badmi *et al.*, 2018). However, stem cross-sections of the *iqd10* single mutants and the *i9 i10*

336   double mutant did not show the *irregular xylem* (*irx*) phenotype observed in secondary cell

337   wall mutants such as *irx14* (Fig. S6a). Furthermore, *iqd* stems had normal monosaccharide

338   composition (Fig. S6b), while *irx14* stems were xylan-deficient as previously described

339   (Brown *et al.*, 2007). *IQD9* and *IQD10* are thus not indispensable for the formation of xylem

340   cells with thick secondary cell walls, or their functions could be masked by other IQDs.

341

342   **IQD9 proteins associate with MTs and interact with KLCR1**

343   To determine the subcellular localization of IQD9 proteins, we first co-expressed IQD9-

344   GFP fusion proteins and the MT marker RFP-TUB6 in *N. benthamiana* leaf epidermal cells.

345   IQD9-GFP localized in striated arrays that overlapped with RFP-TUB6 at the cell cortex (Fig.

346   S7), and could be abolished by treating cells with MT-depolymerizing oryzalin. Next, we co-

347   expressed IQD9-GFP with mCherry-tagged KLCR1 (mCherry-KLCR1) in *N. benthamiana*

348   and found that they were co-localized in arrays resembling MTs (Fig. 4a–c). IQD9 and

349   KLCR1 still co-localized when their striated patterns were disassembled by oryzalin

350   treatment (Fig. 4c–e). We validated that these two proteins physically interact using co-

351   immunoprecipitation (co-IP). IQD9-GFP and RFP-tagged KLCR1 (RFP-KLCR1) proteins

352   were expressed in *N. benthamiana* leaves, extracted and purified by GFP-trap beads. Western

353   blotting showed that all recombinant proteins were present in the input fractions (Fig. 4f),

354   before the addition of the GFP-binding beads. RFP-KLCR1 proteins were detected on GFP-

355   Trap beads only when co-expressed with IQD9-GFP, but not with GFP alone. Therefore,

356   IQD9 proteins physically interacted with KLCR1 *in vivo* and were closely associated with

357   cortical MTs.

13
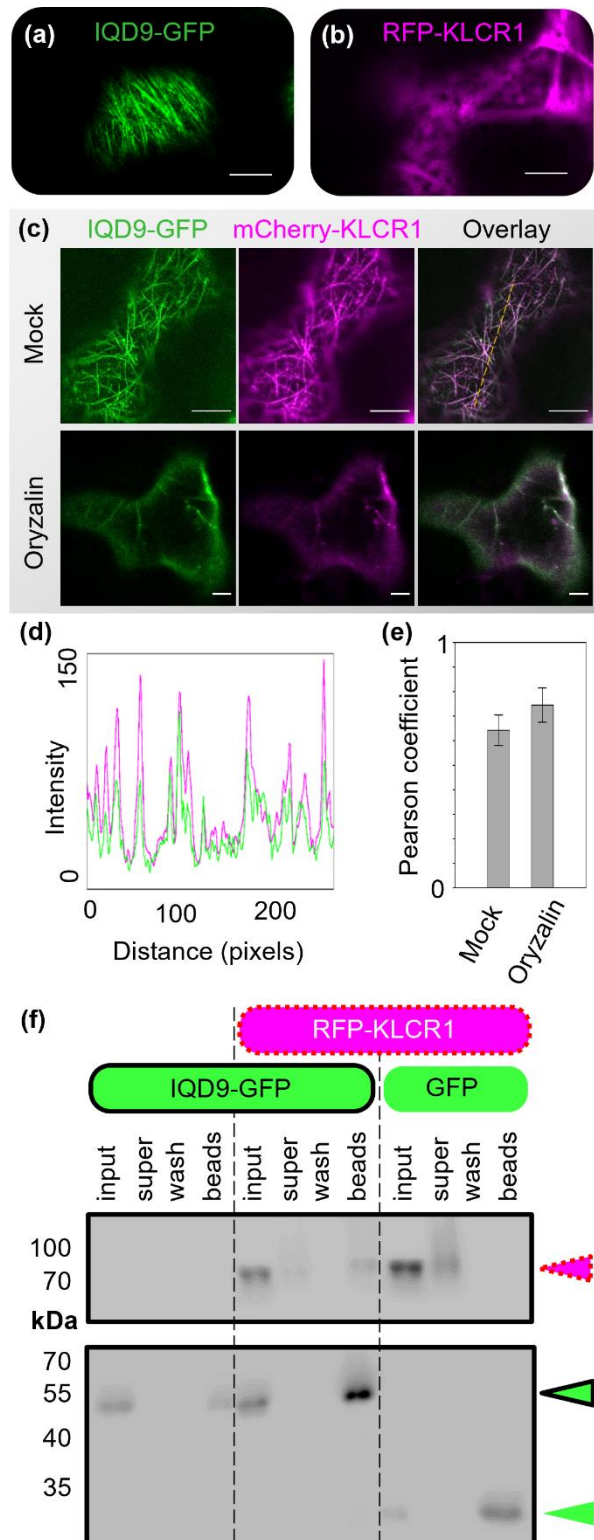
Fig. 4 IQD9 co-aligns and interacts with KLCR1. (a) IQD9-GFP localized in cortical arrays in *N. benthamiana* cells. (b) RFP-KLCR1 shows diffuse localization when overexpressed on its own in tobacco. (c) Subcellular co-localization of IQD9-GFP and mCherry-KLCR1 in the mock and oryzalin-treated tobacco epidermal cells. Both transiently expressed proteins were oryzalin-sensitive. (d) Fluorescent intensity plot along the dashed line in (c). Bars = 10 μm. (e) Pearson correlation coefficient between IQD9-GFP and mCherry-KLCR1 in (c), n=5 cells from 5 independent treatments. (f) Co-IP of proteins transiently expressed in tobacco leaves. Colored triangles marked the expected size of each protein. Labels: Input (protein supernatant before adding the GFP-Trap beads); Super (unbound supernatant after bead incubation); Wash (Supernatant from last wash step); Beads (co-IP proteins that tightly bind GFP-Trap).

358

359

Localization of IQD9-GFP during mucilage biosynthesis

To investigate the distribution of IQD9-GFP in Arabidopsis, we examined its subcellular localization under the control of its native promoter in the complemented *iqd9* line, which rescued the mucilage defects (Fig. 1). While undetectable in young seedlings, IQD9-GFP

14

364 fluorescence was evident during seed coat development (Fig. S8a), particularly at the peak

365 stage of mucilage biosynthesis. Z-stack maximum projections displayed IQD9-GFP proteins

366 in MT arrays, near the PM and inside the nucleus (Fig. 5a). IQD9-GFP displayed circular

367 arrays around the cytoplasmic column, resembling previously described CESA trajectories

368 during mucilage production (Griffiths *et al.*, 2015). At SCE cell boundaries, IQD9-GFP

369 proteins co-localized with the PM stained by FM4-64. Time-lapse imaging revealed that

370 IQD9-GFP proteins were static (the vertical lines in kymograph; Fig. 5b), as previously noted

371 for KLCR/CMU proteins (Liu *et al.*, 2016). Highly immobile KLCR1-GFP proteins,

372 expressed under its native promoter in the complemented *klcr1* line, were also associated

373 with both MTs and PM throughout SCE development (Fig. S8b), but lacked the nuclear

374 localization observed for IQD9-GFP. In cross-sectional views of live SCE cells, both IQD9-

375 GFP and KLCR1-GFP were localized primarily as striated arrays adjacent to the mucilage

376 pocket (Fig. 5c,d).
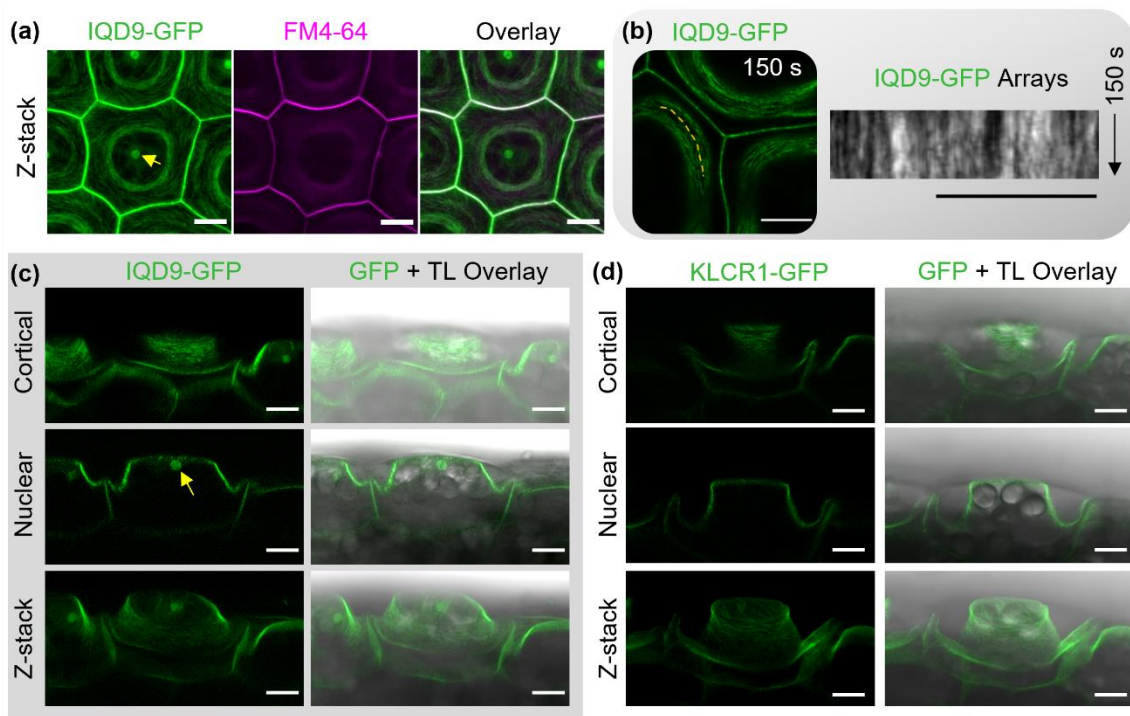
Fig. 5 IQD9 and KLCR1 localization during mucilage biosynthesis in complemented lines.
(a) Z-stack maximum projection of IQD9-GFP SCE cells stained with FM4-64 at 7 DPA. IQD9 is localized at the plasma membrane, MTs and in a nuclear body (arrow). (b) Time-lapse of IQD9-GFP and kymograph along the dashed line. (c) Cross-sectional views of SCE cells expressing IQD9-GFP. The arrow marks a nuclear compartment. (d) Cross-sectional views of SCE cells expressing KLCR1-GFP during mucilage biosynthesis. Bars = 10 μm.

377

378 *IQD9* **maintains MT organization in SCE cells**

379 Proper MT organization is essential for the establishment of mucilage architecture. The

380 MT marker RFP-TUB6, which formed circular arrays around the cytoplasmic column of SCE

15

381   cells at 7 DPA (Yang *et al.*, 2019), was introduced into the *iqd9-1* mutant by crossing. In

382   contrast to the WT background, circular MT arrays were undetectable in all *iqd9* SCE cells

383   expressing RFP-TUB6 (Fig. 6). While MT organization was severely disrupted in the seed

384   coat, both WT and *iqd9* displayed transversely oriented RFP-TUB6 arrays in hypocotyl

385   epidermal cells (Fig. S9), despite some variation in fluorescence intensity. Therefore, the

386   distribution of cortical MTs in the seed coat depends heavily on *IQD9*, while cytoskeleton

387   organization in other tissues likely requires additional *IQDs*.
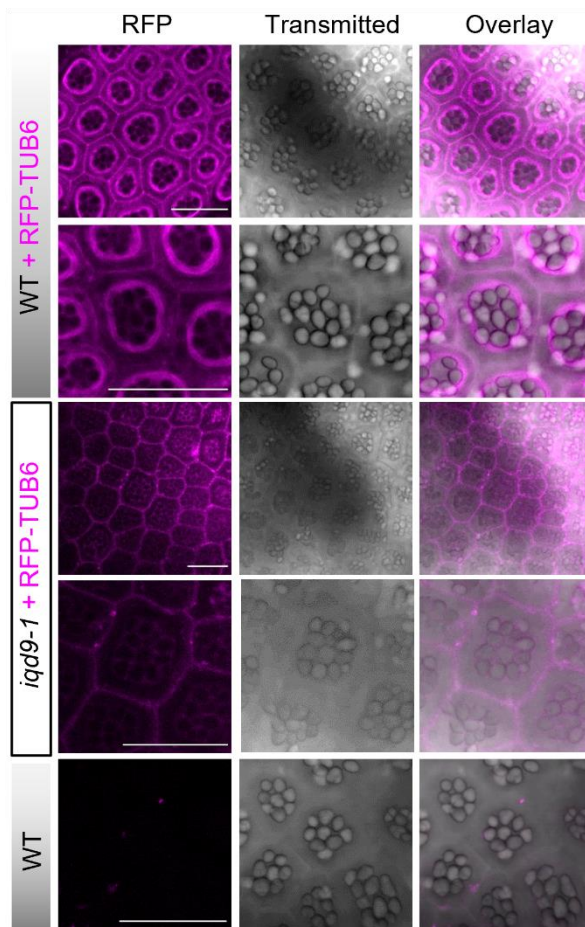
Fig. 6 MT organization was impaired in *iqd9* SCE cells. Z-stack maximum projections of RFP-TUB6 in the SCE cells at 7 DPA stage. RFP-TUB6 cortical arrays formed in the WT background but not in *iqd9* SCE cells. WT cells without RFP-TUB6 served as a negative control. Bars = 50 μm.

388

389   **The loss of *IQD9* reduces CESA3 velocity**

390   CESA3 is a key subunit of the CSC that polarly deposits cellulose in seed mucilage

391   pockets (Griffiths *et al.*, 2015). Since cellulose distribution is disordered in *iqd9* mucilage

392   (Fig. 3), we hypothesized that IQD9 influences CSC motility at the cell cortex. Consistent

393   with previous results (Griffiths *et al.*, 2015), time-lapse images revealed GFP-CESA3

394   proteins moved in a unidirectional, clockwise manner around the cytoplasmic column of SCE

395   cells (Fig. 7). While this pattern was still present, the velocity of GFP-CESA3 particles

396   decreased from 135.9 ± 8.2 nm min^{-1} in WT cells to only 92.8 ± 17.3 nm min^{-1} in *iqd9* (mean

397   $\pm$ SD; at least 170 measurements of 9 cells from 3 plants per genotype). Consistent with their

398   mucilage staining phenotypes (Fig. 1, Fig. S2 and Fig. S3), the movement of GFP-CESA3

399   was also reduced in *trm4* cells, akin to *iqd9* (Fig. 7). In these mutant seeds, CSC movement

400   appeared to be uncoupled from MTs, a behavior previously described for CESA proteins in

401   *klcr* (*cmu*) mutants (Liu *et al.*, 2016), but could not be monitored in greater detail due to the

402   severe disruption of RFP-TUB6 localization in SCE cells (Fig. 6; Yang *et al.*, 2019). Taken

403   together, IQD9 is a novel protein required for seed mucilage biosynthesis by maintaining

404   cortical MT arrays and the speed of CESA movement, which influence cellulose distribution.
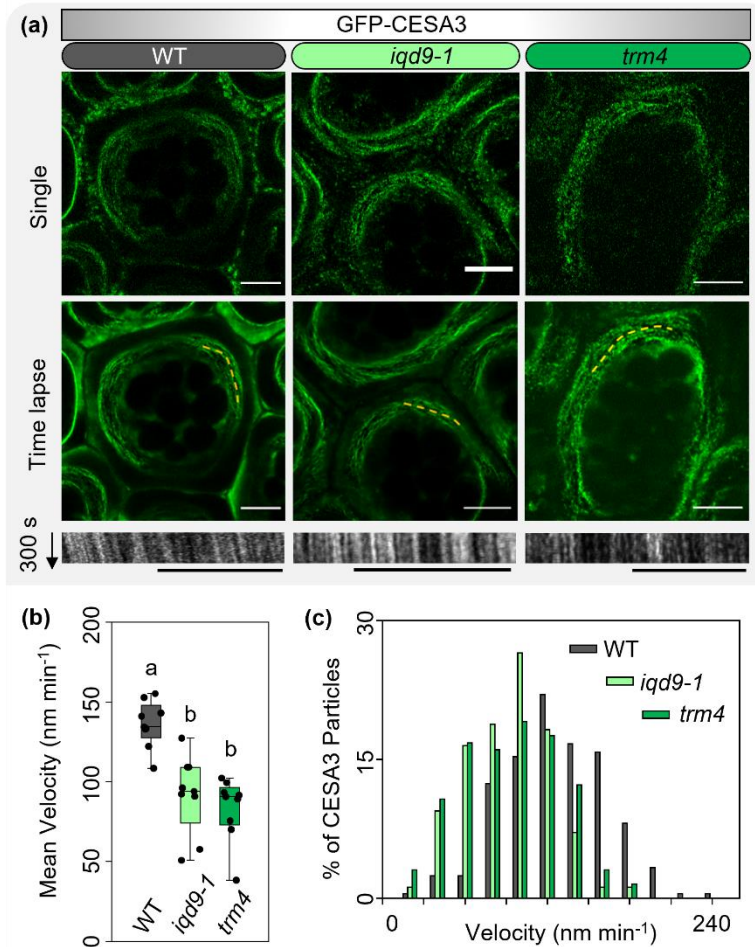
Fig. 7 *IQD9* and *TRM4* enhance the velocity of GFP-CESA3 proteins. (a) Single and time-lapse images (acquired every 5 s for 300 s) of GFP-CESA3 in WT, *iqd9* and *trm4* SCE cells at 7 DPA. The bottom row shows kymographs of GFP-CESA3 from dashed lines in the middle row. Bars = 10 μm. (b) Mean GFP-CESA3 velocity in 9 cells from three plants per genotype. Letters label significant differences (one-way ANOVA with Tukey test, P< 0.01). (c) Distribution of GFP-CESA3 velocities for analyzed particles (N=209 for WT, 170 for *iqd9* and 131 for *trm4*).

405

Discussion

406   In the past decade, SCE cells have become a popular model to identify and study cell

407

408   wall regulators as well as carbohydrate-active enzymes. Dozens of mucilage-related genes

409   have been gradually characterized in Arabidopsis (Voiniciuc *et al.*, 2015c; Šola *et al.*, 2019),

410   primarily through forward and reverse genetic screens. In addition to mutants generated in the

411   laboratory, the architecture of mucilage β-glucans was found to vary dramatically in natural

412   populations of *Arabidopsis thaliana* (Sullivan *et al.*, 2011; North *et al.*, 2014; Voiniciuc *et*

413   *al.*, 2016). The Arabidopsis research findings have been accompanied by advances in the

17

414   mucilage structure of food crops such as *Linum usitatissimum* (flax; Viudes *et al.*, 2020) and

415   *Plantago ovata* (psyllium; (Cowley & Burton, 2021), which contain a higher proportion of

416   non-pectic polymers. Despite the evolution of various mucilage traits within the *Brassicaceae*

417   family (Viudes *et al.*, 2021), how MTs regulate the intricate organization of this specialized

418   secondary cell wall has remained a relatively blank slate. The Arabidopsis genome encodes

419   hundreds of putative MT-associated proteins, but only MOR1 and TRM4 were previously

420   shown to influence seed mucilage synthesis (McFarlane *et al.*, 2008; Hamada, 2014; Yang *et*

421   *al.*, 2019). Additional MT-associated proteins (e.g. CSI1/POM2; CC1; IQD13 and

422   KLCRs/CMUs) involved in cell wall biosynthesis were characterized in other tissues (Li *et*

423   *al.*, 2012; Bringmann *et al.*, 2012b; Endler *et al.*, 2015; Liu *et al.*, 2016; Sugiyama *et al.*,

424   2017), so the players that guide mucilage biosynthesis remained unclear.

425

426   IQD9 sustains MT organization during specialized cell wall deposition

427   In this study, we discovered that IQD9 and its interactor KLCR1 localize to cortical

428   arrays that resemble the circular paths of MTs (Fig. 6) and multiple CESAs (Griffiths *et al.*,

429   2015) during mucilage biosynthesis. IQD9 co-localized with MTs and was sensitive to their

430   depolymerization by oryzalin, suggesting that IQD9 may be capable of directly binding MTs

431   like other family members. The DUF4005 domain of IQD16 was recently shown to mediate

432   MT binding *in vivo* as well as *in vitro* (Li *et al.*, 2021). As one of the shortest family members

433   (Abel *et al.*, 2005), IQD9 lacks the DUF4005 domain but contains a region similar to the

434   MT2 domain of IQD13 (Fig. S1c), which is sufficient for MT localization *in vivo* (Sugiyama

435   *et al.*, 2017). The highly immobile IQD9 proteins could function similarly to KLCR1/CMU1,

436   its binding partner (Fig. 4), to stabilize the cortical MT arrays of SCE cells and sustain CSC

437   speed during cellulose deposition. Consistent with this hypothesis, oryzalin treatment of SCE

438   cells severely disrupted the trajectory and velocity of GFP-CESA3 (Griffiths *et al.*, 2015).

439   The reduced velocity of CESA3-containing CSCs in *iqd9* and *trm4* SCE cells (Fig. 7) shows

440   that multiple classes of proteins are required to shape the circular MT arrays and cellulose

441   distribution.

442

443   MT organization primarily affects cellulose distribution in seed mucilage

444   In Arabidopsis, SCE cells display MT and CSC dynamics that are considerably different

445   from those of hypocotyl and protoxylem vessels (Griffiths *et al.*, 2015; Watanabe *et al.*, 2015;

446   Griffiths & North, 2017), which serve as primary and secondary cell wall models. Both

447   hypocotyl or protoxylem cells show transverse MTs arrays or bundles, aligned with

448   bidirectional movement of CSCs in the PM. The velocities of CSCs during cellulose

449   deposition range from 200–300 nm min^{-1} in the hypocotyl to 300–400 nm min^{-1} in the

450   protoxylem. By contrast, SCE cells display circular MT arrays around the columella, aligned

451   with unidirectional movement of CSCs with a velocity of 80 to 120 nm min^{-1} (Fig. 7,

452   Griffiths *et al.*, 2015). These unique MT pattern and CSC movements could lead to the

453   polarized deposition of unusual cellulosic coils, which unwind with the expansion of pectin

454   polymers during Arabidopsis seed hydration (Šola *et al.*, 2019). Cytoskeletal defects in *iqd9*,

455   *klcr1*, or *trm4* mutants could slow CSC movement to result in shorter cellulose microfibrils

456   that cannot extend to form long ray-like structures during mucilage release. The compact

457   mucilage phenotypes of MT-related mutants and galactoglucomannan-deficient seeds such as

458   *muci10* could be explained by similar deficiencies in the assembly of cellulose chains (Yu *et*

459   *al.*, 2014; Voiniciuc *et al.*, 2015b; Griffiths & North, 2017; Yang *et al.*, 2019),

460   Since relatively abundant MTs line the PM of the mucilage pocket where mucilage

461   secretion occurs (McFarlane *et al.*, 2008), MTs could also potentially target the secretion of

462   pectin and hemicelluloses to the apoplast. However, a temperature-sensitive mutation of

463   *MOR1* partially disrupted mucilage release without clearly affecting the secretion of vesicles

464   to the mucilage pocket and mucilage polymer accumulation (McFarlane *et al.*, 2008). Despite

465   severely disrupted RFP-TUB6 localization in SCE cells (Fig. 6; Yang *et al.*, 2019), the *iqd9*

466   and *trm4* seeds released matrix polysaccharides with a composition that was similar to WT

467   (Fig. 2). Even though the *iqd10-1* mutation partially reduced certain monosaccharides (Fig.

468   2), the mucilage released from these seeds showed a WT-like appearance (Figs. 1 and 3).

469   Therefore, cortical MTs appear to have a relatively minor impact on the incorporation of

470   pectin and hemicelluloses into the mucilage pockets of SCE cells. Unaltered mucilage

471   adherence to the surface of *iqd9*, *klcr1* and *trm4* seeds is likely mediated by the presence of

472   xylan (Voiniciuc *et al.*, 2015a; Ralet *et al.*, 2016), the SOS5 arabinogalactan protein and the

473   receptor-like kinase FEI2 (Harpaz-Saad *et al.*, 2011; Griffiths *et al.*, 2016; Šola *et al.*, 2019).

474

475   **IQD, KLCR, and TRM proteins have interconnected functions**

476   Our results and recently published findings indicate that distinct IQD proteins function

477   in a tissue-specific manner by interacting with KLCR proteins and have potentially

478   overlapping roles with TRM scaffolding proteins. Based on double mutant analyses (Figs. S2

479   and S3), the roles of *IQD9* in SCE cells are nearly identical to those of *KLCR1* and *TRM4*.

480   Therefore, the encoded proteins could be associated as part of a single complex or pathway at

481   the cell cortex. Some Arabidopsis IQDs (GFP-IQD1 or GFP-IQD2) can recruit KLCR1 to

482   MTs when transiently co-expressed in tobacco cells (Bürstenbinder *et al.*, 2013; Zang *et al.*,

483   2021). The MT recruitment is consistent with our results for the transient expression of

484   IQD9-GFP and KLCR1 (which behaves similarly when tagged with either RFP or mCherry),

485   even though KLCR1/CMU1 alone can at least partially bind MTs (Liu *et al.*, 2016; Zang *et*

486   *al.*, 2021). Furthermore, the KLCR1-IQD2 pair was recently shown to interact with the actin

487   binding protein NET3C to modulate the shape of the endoplasmic reticulum at PM contact

488   sites (Zang *et al.*, 2021). We hypothesize that IQD9, KLCR1, TRM4 could be an integral part

489   of an expanding group of proteins (Polko & Kieber, 2019) that support PM-bound CSC

490   movement along the orientation of MT tracks. IQDs are hypothesized to function as scaffolds

491   and may be modified by TON1/TRM/PP2A (TTP)-mediated dephosphorylation (Kumari *et*

492   *al.*, 2021). Via IQ67-domain-mediated calmodulin binding (Abel *et al.*, 2005), IQDs could

493   also participate in Ca^{2+} signaling to ultimately influence plant cell wall dynamics.

494

495   **Intriguing roles of IQDs during secondary cell wall formation**

496   Even though *IQD9* and *IQD10* promoters were active in both vegetative and

497   reproductive organs (Fig. S1), *IQD9* was indispensable only for the organization of seed

498   mucilage polysaccharides (Figs. 1–3). While the expression of IQD9-GFP under its native

499   promoter was detected only in the general seed coat (Fig. 5 and Fig. S4), KLCR1-GFP was

500   expressed more ubiquitously in complemented lines. The transcription of *IQD9*, *IQD10* and

501   *IQD13* was previously associated with secondary cell wall biosynthesis (Mutwil *et al.*, 2008).

502   Even though we detected transcriptional activity in the vasculature (Fig. S1), the absence of

503   *IQD9* and/or *IQD10* did not cause *irx* phenotypes found in stems with defective cellulose-

504   hemicellulose networks (Fig. S6; Brown *et al.*, 2007). Their vascular functions could be

505   masked by the expression of related genes such as *IQD13*, which was already shown to

506   modulate MT organization during xylem cell formation (Sugiyama *et al.*, 2017). In poplar,

507   the down-regulation of *PdIQD10* during wood formation increased the tree height, diameter

508   and relative cellulose content (Badmi *et al.*, 2018). Since PdIQD10 interacted with PdKLCRs

509   and could be directed to the nucleus, the elevated cellulosic biomass of the transgenic trees

510   suggests that IQD-KLCRs participate in a tight feedback-loop that regulates cellulose

511   biosynthesis (Badmi *et al.*, 2018). In Arabidopsis, multiple *IQDs* likely have redundant roles

512   during stem development so higher-order mutants would be needed to decipher how IQD-

513   KLCR are involved in signaling pathways or in direct interactions with secondary wall CSCs.

514

515   **Future avenues to tailor cellulose deposition**

516   The localization of soluble IQD9 and KLCR1/CMU1 (Fig. 5, Liu *et al.*, 2016) proteins

517   near or at the PM suggests that they could interact with membrane-bound CSC components,

518   which travel in a spiral pattern during mucilage synthesis (Griffiths *et al.*, 2015). TRM4 was

519   previously shown to maintain MT organization and directly bind CESA3 (Yang *et al.*, 2019)

520   to enhance its mobility (Fig. 7). Although the mechanism that connects IQD9 and KLCR1 to

521   TRM4 requires further investigation, we provide the first evidence that members of these

522   three MT-associated families cooperate to direct cellulose deposition. Additional CSC-related

523   genes are expressed during mucilage production (Griffiths & North, 2017), but their putative

524   roles in mucilage biosynthesis remain to be investigated. Exploring the interactome of IQD9,

525   KLCR1, and TRM4 could reveal novel targets to fine-tune the biosynthesis of cellulose, the

526   most abundant renewable material on our planet. In addition to plant studies, the growing

527   arsenal of proteins found to influence cellulose biosynthesis could be rapidly expressed and

528   engineered in surrogate hosts (Pauly *et al.*, 2019). Yeast species such as *Pichia pastoris* have

529   already been used to express a *Populus* CESA capable of producing cellulose microfibrils *in*

530   *vitro* (Purushotham *et al.*, 2016) and to identify essential protein co-factors for CESA-like

531   enzymes that catalyze hemicellulose elongation (Voiniciuc *et al.*, 2019). Therefore, synthetic

532   biology advances combined with attractive plant models, such as the Arabidopsis SCE cells,

533   provide exciting avenues to refine the fibers that shape plants and many industrial products.

534

Acknowledgements

544

Authors Contributions

546   C.V. and K.B. conceived the project. B.Y. performed most of the experiments under C.V.'s

547   supervision. G.S. and K.B. contributed genetic materials and performed RT-PCR, GUS and

548   co-IP assays. B.Y. and C.V. analyzed data and wrote the manuscript with input from all authors.

549

References

550 **Abel S, Savchenko T, Levy M**. **2005**. Genome-wide comparative analysis of the IQD gene families in Arabidopsis thaliana and Oryza sativa. *BMC Evolutionary Biology* **5**: 72.

Ambrose C, Allard JF, Cytrynbaum EN, Wasteneys GO. **2011**. A CLASP-modulated cell edge barrier mechanism drives cell-wide cortical microtubule organization in Arabidopsis. *Nature Communications* **2**: 430.

Anderson CT, Carroll A, Akhmetova L, Somerville C. **2010**. Real-Time Imaging of Cellulose Reorientation during Cell Wall Expansion in Arabidopsis Roots. *Plant Physiology* **152**: 787–796.

Badmi R, Payyavula RS, Bali G, Guo H-B, Jawdy SS, Gunter LE, Yang X, Winkeler KA, Collins C, Rottmann WH, *et al.* 2018. A New Calmodulin-Binding Protein Expresses in the Context of Secondary Cell Wall Biosynthesis and Impacts Biomass Properties in Populus. *Frontiers in Plant Science* **9**.

Ben-Tov D, Abraham Y, Stav S, Thompson K, Loraine A, Elbaum R, de Souza A, Pauly M, Kieber JJ, Harpaz-Saad S. **2015**. COBRA-LIKE2, a Member of the Glycosylphosphatidylinositol-Anchored COBRA-LIKE Family, Plays a Role in Cellulose Deposition in Arabidopsis Seed Coat Mucilage Secretory Cells ,. *Plant Physiology* **167**: 711–724.

Ben-Tov D, Idan-Molakandov A, Hugger A, Ben-Shlush I, Günl M, Yang B, Usadel B, Harpaz-Saad S. **2018**. The role of COBRA-LIKE 2 function, as part of the complex network of interacting pathways regulating Arabidopsis seed mucilage polysaccharide matrix organization. *The Plant Journal* **94**: 497–512.

Bringmann M, Landrein B, Schudoma C, Hamant O, Hauser M-T, Persson S. **2012a**. Cracking the elusive alignment hypothesis: the microtubule–cellulose synthase nexus unraveled. *Trends in Plant Science* **17**: 666–674.

Bringmann M, Li E, Sampathkumar A, Kocabek T, Hauser M-T, Persson S. **2012b**. POM-POM2/CELLULOSE SYNTHASE INTERACTING1 Is Essential for the Functional Association of Cellulose Synthase and Microtubules in *Arabidopsis*. *The Plant Cell* **24**: 163–177.

Brown DM, Goubet F, Wong VW, Goodacre R, Stephens E, Dupree P, Turner SR. **2007**. Comparison of five xylan synthesis mutants reveals new insight into the mechanisms of xylan synthesis. *The Plant Journal* **52**: 1154–1168.

Bürstenbinder K, Möller B, Plötner R, Stamm G, Hause G, Mitra D, Abel S. **2017**. The IQD Family of Calmodulin-Binding Proteins Links Calcium Signaling to Microtubules, Membrane Subdomains, and the Nucleus. *Plant Physiology* **173**: 1692–1708.

Bürstenbinder K, Savchenko T, Müller J, Adamson AW, Stamm G, Kwong R, Zipp BJ, Dinesh DC, Abel S. **2013**. Arabidopsis Calmodulin-binding Protein IQ67-Domain 1 Localizes to Microtubules and Interacts with Kinesin Light Chain-related Protein-1. *Journal of Biological Chemistry* **288**: 1871–1882.

Cowley JM, Burton RA. **2021**. The goo-d stuff: Plantago as a myxospermous model with

590   modern utility. *New Phytologist* **229**: 1917–1923.

591   **Crowell EF, Timpano H, Desprez T, Franssen-Verheijen T, Emons A-M, Höfte H,**
592   **Vernhettes S**. **2011**. Differential Regulation of Cellulose Orientation at the Inner and Outer
593   Face of Epidermal Cells in the *Arabidopsis* Hypocotyl. *The Plant Cell* **23**: 2592–2605.

594   **Desprez T, Juraniec M, Crowell EF, Jouy H, Pochylova Z, Parcy F, Hofte H, Gonneau M,**
595   **Vernhettes S**. **2007**. Organization of cellulose synthase complexes involved in primary cell
596   wall synthesis in Arabidopsis thaliana. *Proceedings of the National Academy of Sciences* **104**:
597   15572–15577.

598   **Duncombe SG, Barnes WJ, Anderson CT**. **2020**. Chapter 11 - Imaging the delivery and
599   behavior of cellulose synthases in Arabidopsis thaliana using confocal microscopy. In:
600   Anderson CT, Haswell ES, Dixit R, eds. Plant Cell Biology. Methods in Cell Biology.
601   Academic Press, 201–213.

602   **Endler A, Kesten C, Schneider R, Zhang Y, Ivakov A, Froehlich A, Funke N, Persson S**.
603   **2015**. A Mechanism for Sustained Cellulose Synthesis during Salt Stress. *Cell* **162**: 1353–1364.

604   **Foster CE, Martin TM, Pauly M**. **2010**. Comprehensive Compositional Analysis of Plant
605   Cell Walls (Lignocellulosic biomass) Part II: Carbohydrates. *Journal of Visualized*
606   *Experiments*: 1837.

607   **Ganguly A, Zhu C, Chen W, Dixit R**. **2020**. FRA1 Kinesin Modulates the Lateral Stability
608   of Cortical Microtubules through Cellulose Synthase–Microtubule Uncoupling Proteins. *The*
609   *Plant Cell* **32**: 2508–2524.

610   **Gantner J, Ordon J, Ilse T, Kretschmer C, Gruetzner R, Löfke C, Dagdas Y,**
611   **Bürstenbinder K, Marillonnet S, Stuttmann J**. **2018**. Peripheral infrastructure vectors and
612   an extended set of plant parts for the Modular Cloning system. *PLOS ONE* **13**: e0197185.

613   **Grefen C, Chen Z, Honsbein A, Donald N, Hills A, Blatt MR**. **2010**. A Novel Motif Essential
614   for SNARE Interaction with the K+ Channel KC1 and Channel Gating in *Arabidopsis*. *The*
615   *Plant Cell* **22**: 3076–3092.

616   **Griffiths JS, Crepeau M-J, Ralet M-C, Seifert GJ, North HM**. **2016**. Dissecting Seed
617   Mucilage Adherence Mediated by FEI2 and SOS5. *Frontiers in Plant Science* **7**: 1–13.

618   **Griffiths JS, North HM**. **2017**. Sticking to cellulose: exploiting Arabidopsis seed coat
619   mucilage to understand cellulose biosynthesis and cell wall polysaccharide interactions. *New*
620   *Phytologist* **214**: 959–966.

621   **Griffiths JS, Šola K, Kushwaha R, Lam P, Tateno M, Young R, Voiniciuc C, Dean G,**
622   **Mansfield SD, DeBolt S, *et al.*** **2015**. Unidirectional Movement of Cellulose Synthase
623   Complexes in Arabidopsis Seed Coat Epidermal Cells Deposit Cellulose Involved in Mucilage
624   Extrusion, Adherence, and Ray Formation. *Plant Physiology* **168**: 502–520.

625   **Griffiths JS, Tsai AYL, Xue H, Voiniciuc C, Šola K, Seifert GJ, Mansfield SD, Haughn**
626   **GW**. **2014**. SALT-OVERLY SENSITIVE5 mediates arabidopsis seed coat mucilage
627   adherence and organization through pectins. *Plant Physiology* **165**: 991–1004.

628   **Gutierrez R, Lindeboom JJ, Paredez AR, Emons AMC, Ehrhardt DW**. **2009**. Arabidopsis

23

629 cortical microtubules position cellulose synthase delivery to the plasma membrane and interact
630 with cellulose synthase trafficking compartments. *Nature Cell Biology* **11**: 797–806.

631 **Hamada T**. **2014**. Microtubule Organization and Microtubule-Associated Proteins in Plant
632 Cells. In: International Review of Cell and Molecular Biology. Elsevier, 1–52.

633 **Harpaz-Saad S, McFarlane HE, Xu S, Divi UK, Forward B, Western TL, Kieber JJ**. **2011**.
634 Cellulose synthesis via the FEI2 RLK/SOS5 pathway and CELLULOSE SYNTHASE 5 is
635 required for the structure of seed coat mucilage in Arabidopsis: Synthesis of cellulose in seed
636 mucilage. *The Plant Journal* **68**: 941–953.

637 **Hu R, Li J, Wang X, Zhao X, Yang X, Tang Q, He G, Zhou G, Kong Y**. **2016**. Xylan
638 synthesized by Irregular Xylem 14 (IRX14) maintains the structure of seed coat mucilage in
639 Arabidopsis. *Journal of Experimental Botany* **67**: 1243–1257.

640 **Karimi M, Inzé D, Depicker A**. **2002**. GATEWAY vectors for Agrobacterium-mediated plant
641 transformation. *Trends in Plant Science* **7**: 193–195.

642 **Kölling M, Kumari P, Bürstenbinder K**. **2019**. Calcium- and calmodulin-regulated
643 microtubule-associated proteins as signal-integration hubs at the plasma membrane-
644 cytoskeleton nexus. *Journal of Experimental Botany* **70**: 387–396.

645 **Kumari P, Dahiya P, Livanos P, Zergiebel L, Kölling M, Poeschl Y, Stamm G, Hermann
646 A, Abel S, Müller S,** *et al.* **2021**. IQ67 DOMAIN proteins facilitate preprophase band
647 formation and division-plane orientation. *Nature Plants*: 1–9.

648 **Li Y, Huang Y, Wen Y, Wang D, Liu H, Li Y, Zhao J, An L, Yu F, Liu X**. **2021**. The
649 domain of unknown function 4005 (DUF4005) in an Arabidopsis IQD protein functions in
650 microtubule binding. *Journal of Biological Chemistry* **297**: 100849.

651 **Li S, Lei L, Somerville CR, Gu Y**. **2012**. Cellulose synthase interactive protein 1 (CSI1) links
652 microtubules and cellulose synthase complexes. *Proceedings of the National Academy of
653 Sciences* **109**: 185–190.

654 **Liang H, Zhang Y, Martinez P, Rasmussen CG, Xu T, Yang Z**. **2018**. The Microtubule-
655 Associated Protein IQ67 DOMAIN5 Modulates Microtubule Dynamics and Pavement Cell
656 Shape. *Plant Physiology* **177**: 1555–1568.

657 **Liu Z, Schneider R, Kesten C, Zhang Y, Somssich M, Zhang Y, Fernie AR, Persson S**.
658 **2016**. Cellulose-Microtubule Uncoupling Proteins Prevent Lateral Displacement of
659 Microtubules during Cellulose Synthesis in Arabidopsis. *Developmental Cell* **38**: 305–315.

660 **Lloyd C, Hussey P**. **2001**. Microtubule-associated proteins in plants — why we need a map.
661 *Nature Reviews Molecular Cell Biology* **2**: 40–47.

662 **McFarlane HE, Young RE, Wasteneys GO, Samuels AL**. **2008**. Cortical microtubules mark
663 the mucilage secretion domain of the plasma membrane in Arabidopsis seed coat cells. *Planta*
664 **227**: 1363–1375.

665 **Mendu V, Griffiths JS, Persson S, Stork J, Downie AB, Voiniciuc C, Haughn GW, DeBolt
666 S**. **2011**. Subfunctionalization of Cellulose Synthases in Seed Coat Epidermal Cells Mediates
667 Secondary Radial Wall Synthesis and Mucilage Attachment. *Plant Physiology* **157**: 441–453.

24

Mielke S, Zimmer M, Meena MK, Dreos R, Stellmach H, Hause B, Voiniciuc C, Gasperini D. 2021. Jasmonate biosynthesis arising from altered cell walls is prompted by turgor-driven mechanical compression. *Science Advances* **7**: eabf0356.

Mitra D, Klemm S, Kumari P, Quegwer J, Möller B, Poeschl Y, Pflug P, Stamm G, Abel S, Bürstenbinder K. 2019. Microtubule-associated protein IQ67 DOMAIN5 regulates morphogenesis of leaf pavement cells in Arabidopsis thaliana. *Journal of Experimental Botany* **70**: 529–543.

Mutwil M, Obro J, Willats WGT, Persson S. 2008. GeneCAT--novel webtools that combine BLAST and co-expression analyses. *Nucleic Acids Research* **36**: W320–W326.

Nakagawa T, Suzuki T, Murata S, Nakamura S, Hino T, Maeo K, Tabata R, Kawai T, Tanaka K, Niwa Y, *et al.* 2007. Improved Gateway binary vectors: high-performance vectors for creation of fusion constructs in transgenic analysis of plants. *Bioscience, Biotechnology, and Biochemistry* **71**: 2095–2100.

North HM, Berger A, Saez-Aguayo S, Ralet M-C. 2014. Understanding polysaccharide production and properties using seed coat mutants: future perspectives for the exploitation of natural variants. *Annals of Botany* **114**: 1251–1263.

Paredez AR, Somerville CR, Ehrhardt DW. 2006. Visualization of Cellulose Synthase Demonstrates Functional Association with Microtubules. *Science* **312**: 1491–1495.

Pauly M, Gawenda N, Wagner C, Fischbach P, Ramírez V, Axmann IM, Voiniciuc C. 2019. The Suitability of Orthogonal Hosts to Study Plant Cell Wall Biosynthesis. *Plants* **8**: 516.

Polko JK, Barnes WJ, Voiniciuc C, Doctor S, Steinwand B, Hill JL, Tien M, Pauly M, Anderson CT, Kieber JJ. 2018. SHOU4 Proteins Regulate Trafficking of Cellulose Synthase Complexes to the Plasma Membrane. *Current Biology* **28**: 3174-3182.e6.

Polko JK, Kieber JJ. 2019. The Regulation of Cellulose Biosynthesis in Plants. *The Plant Cell* **31**: 282–296.

Purushotham P, Cho SH, Díaz-Moreno SM, Kumar M, Nixon BT, Bulone V, Zimmer J. 2016. A single heterologously expressed plant cellulose synthase isoform is sufficient for cellulose microfibril formation in vitro. *Proceedings of the National Academy of Sciences* **113**: 11360–11365.

Ralet M-C, Crépeau M-J, Vigouroux J, Tran J, Berger A, Sallé C, Granier F, Botran L, North HM. 2016. Xylans Provide the Structural Driving Force for Mucilage Adhesion to the Arabidopsis Seed Coat. *Plant Physiology* **171**: 165–178.

Sedbrook JC, Kaloriti D. 2008. Microtubules, MAPs and plant directional cell expansion. *Trends in Plant Science* **13**: 303–310.

Šola K, Dean GH, Haughn GW. 2019. Arabidopsis Seed Mucilage: A Specialised Extracellular Matrix that Demonstrates the Structure–Function Versatility of Cell Wall Polysaccharides. *Annual Plant Reviews online* **2**: 1085–1116.

Sugiyama Y, Wakazaki M, Toyooka K, Fukuda H, Oda Y. 2017. A Novel Plasma Membrane-Anchored Protein Regulates Xylem Cell-Wall Deposition through Microtubule-

707   Dependent Lateral Inhibition of Rho GTPase Domains. *Current Biology* **27**: 2522-2528.e4.

708   **Sullivan S, Ralet M-C, Berger A, Diatloff E, Bischoff V, Gonneau M, Marion-Poll A,**
709   **North HM**. **2011**. CESA5 Is Required for the Synthesis of Cellulose with a Role in Structuring
710   the Adherent Mucilage of Arabidopsis Seeds. *Plant Physiology* **156**: 1725–1739.

711   **Updegraff DM**. **1969**. Semimicro determination of cellulose inbiological materials. *Analytical*
712   *Biochemistry* **32**: 420–424.

713   **Vellosillo T, Yeats T, Sorek N**. **2015**. Analysis of in vivo Cellulose Biosynthesis in
714   Arabidopsis Cells by Spinning Disk Confocal Microscopy. *Bio-protocol* **5**: e1617–e1617.

715   **Viudes S, Burlat V, Dunand C**. **2020**. Seed mucilage evolution: Diverse molecular
716   mechanisms generate versatile ecological functions for particular environments. *Plant, Cell &*
717   *Environment* **43**: 2857–2870.

718   **Viudes S, Dunand C, Burlat V**. **2021**. Myxospermy Evolution in Brassicaceae: A Highly
719   Complex and Diverse Trait with Arabidopsis as an Uncommon Model. *Cells* **10**: 2470.

720   **Voiniciuc C**. **2016**. Quantification of the Mucilage Detachment from Arabidopsis Seeds. *BIO-*
721   *PROTOCOL* **6**: 1–9.

722   **Voiniciuc C, Dama M, Gawenda N, Stritt F, Pauly M**. **2019**. Mechanistic insights from plant
723   heteromannan synthesis in yeast. *Proceedings of the National Academy of Sciences* **116**: 522–
724   527.

725   **Voiniciuc C, Guenl M, Schmidt MH-W, Usadel B**. **2015a**. Highly Branched Xylan Made by
726   IRX14 and MUCI21 Links Mucilage to Arabidopsis Seeds. *Plant Physiology*: pp.01441.2015.

727   **Voiniciuc C, Günl M**. **2016**. Analysis of Monosaccharides in Total Mucilage Extractable from
728   Arabidopsis Seeds. *Bio-protocol* **6**: e1801–e1801.

729   **Voiniciuc C, Schmidt MH-W, Berger A, Yang B, Ebert B, Scheller HV, North HM, Usadel**
730   **B, Günl M**. **2015b**. MUCILAGE-RELATED10 Produces Galactoglucomannan That
731   Maintains Pectin and Cellulose Architecture in Arabidopsis Seed Mucilage. *Plant Physiology*
732   **169**: 403–420.

733   **Voiniciuc C, Yang B, Schmidt MH-W, Günl M, Usadel B**. **2015c**. Starting to Gel: How
734   Arabidopsis Seed Coat Epidermal Cells Produce Specialized Secondary Cell Walls.
735   *International Journal of Molecular Sciences* **16**: 3452–3473.

736   **Voiniciuc C, Zimmermann E, Schmidt MH-W, Günl M, Fu L, North HM, Usadel B**. **2016**.
737   Extensive Natural Variation in Arabidopsis Seed Mucilage Structure. *Frontiers in Plant*
738   *Science* **7**: 1–14.

739   **Watanabe Y, Meents MJ, McDonnell LM, Barkwill S, Sampathkumar A, Cartwright HN,**
740   **Demura T, Ehrhardt DW, Samuels AL, Mansfield SD**. **2015**. Visualization of cellulose
741   synthases in Arabidopsis secondary cell walls. *Science* **350**: 198–203.

742   **Yang B, Hofmann F, Usadel B, Voiniciuc C**. **2021**. Seed hemicelluloses tailor mucilage
743   properties and salt tolerance. *New Phytologist* **229**: 1946–1954.

744 **Yang B, Voiniciuc C, Fu L, Dieluweit S, Klose H, Usadel B**. **2019**. TRM4 is essential for
745 cellulose deposition in Arabidopsis seed mucilage by maintaining cortical microtubule
746 organization and interacting with CESA3. *New Phytologist* **221**: 881–895.

747 **Yu L, Shi D, Li J, Kong Y, Yu Y, Chai G, Hu R, Wang J, Hahn MG, Zhou G**. **2014**.
748 CELLULOSE SYNTHASE-LIKE A2, a glucomannan synthase, is involved in maintaining
749 adherent mucilage structure in arabidopsis seed. *Plant Physiology* **164**: 1842–1856.

750 **Zang J, Klemm S, Pain C, Duckney P, Bao Z, Stamm G, Kriechbaumer V, Bürstenbinder**
751 **K, Hussey PJ, Wang P**. **2021**. A novel plant actin-microtubule bridging complex regulates
752 cytoskeletal and ER structure at ER-PM contact sites. *Current Biology* **31**: 1251-1260.e4.

753 **Zhang Y, Nikolovski N, Sorieul M, Vellosillo T, McFarlane HE, Dupree R, Kesten C,**
754 **Schneider R, Driemeier C, Lathe R, *et al.* 2016**. Golgi-localized STELLO proteins regulate
755 the assembly and trafficking of cellulose synthase complexes in Arabidopsis. *Nature*
756 *Communications* **7**: 11656.

757

758 **Figure Legends**

759 **Fig. 1** Mutation of *IQD9* and *KLCR1* caused compact mucilage capsule. (a) Expression

760 profiles in the seed eFP browser (Winter *et al.*, 2007; Le *et al.*, 2010), including absolute

761 expression values. Glob. (globular); Cotyl. (cotyledon). (b) UTR, intron and exon structure of

762 candidate genes. The position and the effects of T-DNA insertions were verified using RT-

763 PCR, *ACTIN2* as a reference gene, g as genomic DNA control, and – as no DNA control.

764 Transgene complemented were marked by + *IQD* or + *KLCR*. Scale bars for gene models =

765 1000 bp. (c) RR staining of adherent mucilage capsules after gentle shaking in water. Bars =

766 100 µm. (d) Seed (triangles) and RR-stained mucilage (black dots) area of four biological

767 replicates (>20 seeds each) per genotype. Boxes show the 25–75% quartiles, the median

768 value (inner horizontal line), and whiskers extending to the largest/smallest values. Different

769 letters mark $P < 0.01$ for one-way ANOVA with Tukey test. (e) Absolute amounts of

770 monosaccharides in sequentially-extracted mucilage fractions. Data show mean ±SD of 5

771 biological replicates, and asterisks mark significant changes compared to WT (Student's t-

772 test, $P < 0.001$). See Fig. 2 for detailed composition.

773

774 **Fig. 2** Composition of matrix polysaccharides in seed mucilage extracts. (a) Non-adherent

775 and (b) adherent mucilage polysaccharides were sequentially extracted using water and

776 different mixing intensities. Data show mean + SD of 5 biological replicates (only 3 for

777 *muci10*). Red asterisks and arrows (for galactoglucomannan subunits) mark differences from

778 WT (Student's t-test, $P < 0.0001$).

779

27

780   **Fig. 3** *IQD9* and *KLCR1* are important for cellulose deposition around seed surface. (a) S4B-

781   stained cellulosic rays in mucilage capsules. Bars = 100 µm. (b) The length of cellulosic rays

782   stained with S4B. Boxes show the 25–75% quartiles, the median value (inner horizontal line),

783   and whiskers extending to the largest/smallest values (≥10 measurements per biological

784   replicate). (c) Crystalline cellulose content in whole seeds (5 biological replicates per

785   genotype, except 3 for *muci10*). Different letters in (b) and (c) mark significant changes (one-

786   way ANOVA with Tukey test, $P < 0.01$).

787

788   **Fig. 4** IQD9 co-aligns and interacts with KLCR1. (a) IQD9-GFP localized in cortical arrays

789   in *N. benthamiana* cells. (b) RFP-KLCR1 shows diffuse localization when overexpressed on

790   its own in tobacco. (c) Subcellular co-localization of IQD9-GFP and mCherry-KLCR1 in the

791   mock and oryzalin-treated tobacco epidermal cells. Both transiently expressed proteins were

792   oryzalin-sensitive. (d) Fluorescent intensity plot along the dashed line in (c). Bars = 10 µm.

793   (e) Pearson correlation coefficient between IQD9-GFP and mCherry-KLCR1 in (c), n=5 cells

794   from 5 independent treatments. (f) Co-IP of proteins transiently expressed in tobacco leaves.

795   Colored triangles marked the expected size of each protein. Labels: Input (protein supernatant

796   before adding the GFP-Trap beads); Super (unbound supernatant after bead incubation);

797   Wash (Supernatant from last wash step); Beads (co-IP proteins that tightly bind GFP-Trap).

798

799   **Fig. 5** IQD9 and KLCR1 localization during mucilage biosynthesis in complemented lines.

800   (a) Z-stack maximum projection of IQD9-GFP SCE cells stained with FM4-64 at 7 DPA.

801   IQD9 is localized at the PM, MTs and in a nuclear body (arrow). (b) Time-lapse of IQD9-

802   GFP and kymograph along the dashed line. (c) Cross-sectional views of SCE cells expressing

803   IQD9-GFP. The arrow marks a nuclear compartment. (d) Cross-sectional views of SCE cells

804   expressing KLCR1-GFP during mucilage biosynthesis. Bars = 10 µm.

805

806   **Fig. 6** MT organization was impaired in *iqd9* SCE cells. Z-stack maximum projections of

807   RFP-TUB6 in the SCE cells at 7 DPA stage. RFP-TUB6 cortical arrays formed in the WT

808   background but not in *iqd9* SCE cells. WT cells without RFP-TUB6 served as a negative

809   control. Bars = 50 µm.

810

811   **Fig. 7** *IQD9* and *TRM4* enhance the velocity of GFP-CESA3 proteins.

812   (a) Single and time-lapse images (acquired every 5 s for 300 s) of GFP-CESA3 in WT, *iqd9*

813   and *trm4* SCE cells at 7 DPA. The bottom row shows kymographs of GFP-CESA3 from

814   dashed lines in the middle row. Bars = 10 µm. (b) Mean GFP-CESA3 velocity in 9 cells from

815   three plants per genotype. Letters label significant differences (one-way ANOVA with Tukey

816   test, P< 0.01). (c) Distribution of GFP-CESA3 velocities for analyzed particles (N=209 for

817   WT, 170 for *iqd9* and 131 for *trm4*).